# Whole-brain modeling explains the context-dependent effects of cholinergic neuromodulation

**Carlos Coronel-Oliveros**[1,2,3], **Carsten Gießing**[4], **Vicente Medel**[5, 6], **Rodrigo Cofré**[7,8], **and Patricio Orio**[2,9,*]

[1]Doctorado en Ciencias Mención Biofísica y Biología Computacional, Universidad de Valparaíso, Valparaíso, Chile
[2]Centro Interdisciplinario de Neurociencia de Valparaíso (CINV), Universidad de Valparaíso, Valparaíso, Chile
[3]Latin American Health Brain Institute (BrainLat), Universidad Adolfo Ibáñez, Santiago, Chile
[4]Carl von Ossietzky University of Oldenburg, Department of Psychology, Oldenburg, Germany
[5]University of Sydney, Brain and Mind Centre, Sydney, Australia
[6]Universidad de Chile, Departamento de Neurociencia, Santiago, Chile
[7]Institute of Neuroscience (NeuroPSI), Paris-Saclay University, Centre National de la Recherche Scientifique (CNRS), Gif-sur-Yvette, France
[8]CIMFAV-Ingemat, Facultad de Ingeniería, Universidad de Valparaíso, Valparaíso, Chile
[9]Instituto de Neurociencia, Facultad de Ciencias, Universidad de Valparaíso, Valparaíso, Chile
[*]For correspondence: patricio.orio@uv.cl

## ABSTRACT

Integration and segregation are accepted as two fundamental principles of brain organization. The brain manages the transitions between different functional states, more segregated or integrated, through neuromodulatory systems. Recently computational and experimental works suggest a pro-segregation effect of cholinergic neuromodulation. Here, we studied the effects of the cholinergic system on brain functional connectivity using both empirical fMRI data and computational modeling. First, we analyzed the effects of nicotine on functional connectivity and network topology of healthy subjects during resting-state conditions and during an attentional task. Then, to find causal mechanisms about these changes, we employed a whole-brain neural mass model embedded into a human connectome for simulating the effects of nicotine. We found that nicotine incremented functional segregation in both empirical and simulated data, and the effects are context-dependent: observed during task, but not in resting-state. In-task performance correlates with functional segregation, discovering a link between functional network topology and behavior. In the model, the drug was modeled decreasing both the global coupling and local feedback inhibition parameters of the model, consistent with the known cellular effects of acetylcholine. Also, we found that the regional density of the nicotinic acetylcholine $\alpha_4\beta_2$ receptor explains better the effects of nicotine at the whole-brain level. Our results confirm that cholinergic neuromodulation promotes functional segregation in a context-dependent fashion, and suggest that this segregation is suited for simple visual-attentional tasks. In addition, we propose biophysical mechanisms to simulate cholinergic neuromodulation in whole-brain models.

**Keywords:** Acetylcholine, fMRI, Neuromodulation, Nicotine, Segregation, Whole-brain models

## 1 Introduction

The flexible and adaptive behavior of vertebrate animals in different environmental contexts is partly possible due to the brain macroscale "anatomical architecture" also denoted Structural Connectivity (SC), that quantify the existence of white matter tracts physically interconnecting pairs of brain regions. The brain SC sets the basis for the processing of information by domain-specific systems (segregation), and allows the binding of this specialized processing (integration) to guide adaptive behavior [1]. In fact, integration and segregation are proposed as prominent organizational principles in the brain [2–4], and their balance is a crucial element for the dynamical richness and flexibility of neural activity, necessary for the coherent global functioning of the brain [5, 6].

At the macro-scale level, neural activity can be measured through electroencephalogram (EEG) and functional magnetic resonance imaging (fMRI) recordings, among other techniques. The functional brain organization is typically characterized using pairwise statistical interdependencies between brain areas, building functional connectivity (FC) matrices [7, 8]. When applying graph theoretical approaches to the brain's FC, striking fluctuations on the network topology appear between different

conditions. In particular, a more segregated brain network is related to specific motor tasks, making brain regions more domain-specific [3]. In contrast, a reconfiguration towards the integration of the brain's network is observed in complex tasks and arousal-related states [3, 9]. Interestingly, it has been shown that FC in resting-state (RS) conditions reveals a "default" balance between integration and segregation [3, 10, 11]. This balance changes toward segregation or integration as a function of behavioral tasks [3, 10], or by pathological conditions [12–14]. However, the SC that provides the basis for shaping the brain dynamics, remains fixed during the short time scales that are relevant for cognitive tasks. Thus, how the brain can manage the transitions between different FC patterns, starting from a fixed connectome? One candidate mechanism corresponds to neuromodulatory systems [4].

Neuromodulators change the neuron's response profile without necessarily causing the cell to fire [15, 16], increasing or decreasing the probability of neurons to fire actions potentials. A recent hypothesis points out that the cholinergic and noradrenergic systems are key elements in promoting more segregated and integrated states, respectively [4]. At the behavioral level, acetylcholine is involved in several cognitive processes, such as attention, cue detection, and memory [17]. In the cortex, it has been suggested that acetylcholine could produce a shift from a internal-driven –high influence of excitatory feedback connections– to a sensory-driven processing of information, increasing the precision of sensory coding [18, 19]. Following this idea, the cholinergic system can reduce the influence of long-range feedback connections, through mechanisms that rely on both muscarinic and nicotinic receptors [18, 20, 21]. Also, the cholinergic system can increase the excitability of pyramidal neurons by reducing the somatic feedback inhibition mediated by interneurons [18, 22, 23]. Regarding nicotinic acetylcholine receptors, activation of $\beta_2$-containing receptors by acetylcholine enhances the firing rates of dendritic-targeting gabaergic interneurons –for example, inhibitory Martinotti cells [24, 25]– increasing the inhibitory tone onto apical section of deep layers pyramidal neurons, and interfering with the feedback connections that arrive to that section [18, 21, 26].

Computational and experimental works [9, 27, 28] suggest that the effects of noradrenergic and cholinergic neuromodulation are context-dependent, that is, different during task than in RS. In the case of noradrenaline, its role in promoting functional integration was previously addressed by [9, 10, 29]. At the whole-brain level, several mechanisms have been proposed to explain the effects of acetylcholine [15, 28, 30, 31]. However, there is still no clear relation between context-dependent cholinergic modulation and large scale network topology, as related to the cholinergic effect on promoting functional segregation [4]. A direct link between the empirical data, functional network topology and computational modeling of cholinergic system is missing. This constitutes the focus of the present work.

Here, we analyzed fMRI data previously published in [32], in both RS and task conditions (Go/No-Go attentional task), under the effects of nicotine. Specifically, we analyzed the FC using tools from graph theory to quantify integration, as global efficiency, and segregation, as transitivity [33]. Then, we built a whole-brain model from Jansen & Rit neural masses [34] interconnected using a human connectome. fMRI BOLD-like signals were generated from the firing rates of neural masses [35] and simulated FC matrices were computed. The model was fitted to reproduce the empirical FC matrices, minimizing the euclidean between the simulated and empirical FC matrices in each condition (placebo and nicotine) and blocks (RS and task). We simulated the effects of nicotine decreasing the global coupling and feedback inhibition parameters in the model, as suggested previously [28]. The task was simulated by a heterogeneous change in the background input to brain regions. Our simulation results reproduce the context-dependent effects of nicotine, promoting functional segregation during task but not in RS.

At the behavioral level, we correlated the performance of the subjects in the Go/No-Go task with metrics computed from the empirical FC matrices. We found that segregation is a signature of in-task performance, showing a link between functional network topology and behavior. Finally, under the hypothesis that nicotine decreases global correlations, we verified if the regional density of cholinergic-related receptors obtained by positron emission tomography (PET) [36–41] correlates with regional changes in FC. We observed that changes in nodal strength correlate with both the nodal SC strength, and the regional density of the $\alpha_4\beta_2$ nicotinic acetylcholine receptor. Further, the $\alpha_4\beta_2$ receptor density map better explains the effects of nicotine on FC in the task condition.

Overall, those findings contribute to the understanding of how cholinergic neuromodulation promotes the context-dependent changes in functional network topology, and constitutes the first approach to characterize the effects of this system combining empirical fMRI data, computational modeling and behavioral measures.

## 2 Methods

### 2.1 Ethics statement

Experimental data used in this work was previously collected in [32], where the ethical approval was obtained from the ethics committee of the German Psychological Association. Participants wrote informed consent for all procedures, which follow the principles of the Declaration of Helsinki.

### 2.2 Subjects and nicotine administration

The study involves a re-analysis of a previously published dataset [32]. Eighteen healthy right-handed cigarette smokers were studied in a double-blind, randomized, placebo-controlled, crossover design in which once nicotine was delivered in the form of a 4 mg nicotine polacrilex gum (Nicorette, McNeil AB) and once a placebo in the form of a taste- and size-matched gum. The gum was chewed for 30 minutes; then the scanning started immediately. Subjects were asked to refrain from smoking 2 hours before the experiment.

### 2.3 Paradigm and task

The placebo and nicotine session were separated by at least 2 weeks and each session was divided into different time periods in which resting-state oscillations or task activations were measured using fMRI. Three resting-state blocks comprising 256, 256, and 512 scans were measured alternately with two task blocks of 339 scans. During task blocks, participants performed a reversed version of the continuous performance test, measuring processes related to attention and vigilance [42]. During resting-state periods, participants were instructed to lie within the scanner, to keep their eyes open and to attend to a centrally presented visual stimulus.

### 2.4 fMRI data acquisition

Scanning was performed with a Siemens MAGNETOM Sonata MRI system (1.5 T). 1729 T2*-weighted echo-planar images with BOLD contrast were measured with a repetition time of 1.5 s and echo time of 50 ms. Detailed information on the investigated sample, nicotine administration, the paradigm, and the fMRI data acquisition can be found in [32].

### 2.5 Preprocessing and time series analysis

Preprocessing steps consisted in slice timing offsets correction, removal of head movements artifacts by alignment to the first volume, and spatial normalization to standard stereotaxic MNI space. Then, time series were extracted using the AAL90 parcellation [43]. The fMRI BOLD time series were band-pass filtered between 0.01 and 0.1 Hz with a 3rd order Bessel filter, and then used to build the FC matrices –employing pairwise Pearson correlations– from which the subsequent analysis of functional network properties was performed.

Average volumetric PET images were collected for 3 different cholinergic receptors and transporters across 5 studies with open-dataset [40], which include nicotinic $\alpha_4\beta_2$ [36], muscarinic $M_1$ [41], and the vesicular acetylcholine transporter (VAChT) [37, 39, 40].

### 2.6 Whole-brain neural mass model

We simulated neuronal activity using the Jansen & Rit neural mass model [34, 44]. In this model, a brain area consists of three populations of neurons: pyramidal neurons, excitatory and inhibitory interneurons (Fig. 1A). The dynamical evolution of the three populations within the brain areas is modeled by two blocks each. The first block transforms the average pulse density in average postsynaptic membrane potential (which can be either excitatory or inhibitory) (Fig. 1B). This block, denominated post synaptic potential (PSP) block, is represented by an impulse response function. For the excitatory outputs:

$$h_E(t) = \begin{cases} Aate^{-at}, & t \geq 0 \\ 0, & t < 0 \end{cases} \tag{1}$$

and for the inhibitory ones

$$h_I(t) = \begin{cases} Bbte^{-bt}, & t \geq 0 \\ 0, & t < 0, \end{cases} \tag{2}$$

The constants $A$ and $B$ define the maximum amplitude of the PSPs for the excitatory (EPSPs) and inhibitory (IPSPs) cases respectively, while $a$ and $b$ represent the inverse time constants for the excitatory and inhibitory postsynaptic action potentials, respectively. The second block transforms the postsynaptic membrane potential in average pulse density, and is given by a sigmoid function of the form

$$S(v,r) = \frac{\zeta_{max}}{1+e^{r(v_{th}-v)}}, \tag{3}$$

with $\zeta_{max}$ as the maximum firing rate of the neuronal population, $r$ the slope of the sigmoid function, $v_{th}$ the half maximal response of the population, and $v$ their average PSP. Additionally, pyramidal neurons receive an external background input $p(t)$, whose values are taken from a Gaussian distribution with mean $\mu = 4.8$ impulses/s and standard deviation $\sigma = 1$. A

parameter $\beta$ modifies heterogeneously the background input, as a function of the change in nodal strength $\Delta K_i^w$. In the model, each node $i \in [1 \dots n]$ represents a single brain area. The global coupling is scaled by a parameter $\alpha$, and nodes are connected by a structural connectivity matrix $M$ (Fig. 1C). This matrix is derived from a human connectome [45] parcellated in $n = 90$ cortical and subcortical regions with the automated anatomical labeling (AAL90) atlas [43]; the matrix is undirected and takes values between 0 and 1. Because long-range connections are mainly excitatory [46, 47], only links between the pyramidal neurons of a node $i$ with pyramidal neurons of a node $j$ are considered.

The set of equations, for a node $i$, includes the within and between nodes activity

$$\begin{aligned}
\dot{x}_{0,i}(t) &= y_{0,i}(t) \\
\dot{y}_{0,i}(t) &= Aa\left[S(C_2 x_{1,i}(t) - C_4 x_{2,i}(t) + C\alpha z_i(t), r_0)\right] - 2a y_{0,i}(t) - a^2 x_{0,i}(t) \\
\dot{x}_{1,i}(t) &= y_{1,i}(t) \\
\dot{y}_{1,i}(t) &= Aa\left[p(t) + \beta \Delta K_i^w + S(C_1 x_{0,i}(t), r_1)\right] - 2a y_{1,i}(t) - a^2 x_{1,i}(t) \\
\dot{x}_{2,i}(t) &= y_{2,i}(t) \\
\dot{y}_{2,i}(t) &= Bb\left[S(C_3 x_{0,i}(t), r_2)\right] - 2b y_{2,i}(t) - b^2 x_{2,i}(t) \\
\dot{x}_{3,i}(t) &= y_{3,i}(t) \\
\dot{y}_{3,i}(t) &= A\bar{a}\left[S(C_2 x_{1,i}(t) - C_4 x_{2,i}(t) + C\alpha z_i(t), r_0)\right] - 2\bar{a} y_{3,i}(t) - \bar{a}^2 x_{3,i}(t)
\end{aligned} \tag{4}$$

where $x_0$, $x_1$, $x_2$ correspond to the local outputs of the PSP blocks of the pyramidal neurons, and excitatory and inhibitory loops, respectively, and $x_3$ the long-range outputs of pyramidal neurons. The constants $C_1$, $C_2$, $C_3$ and $C_4$ scale the connectivity between the neural populations (see Fig. 1A). We used the original parameter values of Jansen & Rit [34, 44], except for $C_4$: $\zeta_{max} = 5\ \mathrm{s}^{-1}$, $\nu_{th} = 6$ mV, $r_0 = r_1 = r_2 = 0.56\ \mathrm{mV}^{-1}$, $a = 100\ \mathrm{s}^{-1}$, $b = 50\ \mathrm{s}^{-1}$, $A = 3.25$ mV, $B = 22$ mV, $C_1 = C$, $C_2 = 0.8C$, $C_3 = 0.25C$, and $C = 135$. The parameter $C_4$ was defined as a linear function of global coupling: $C_4 = (0.3 + 0.6\alpha)C$. The modification allowed the model to sustain oscillations in a wider range of $\alpha$ values, that is, it preserves the excitation/inhibition (E/I) balance. The term $\beta \Delta K_i^w$ represents an additional heterogeneous input used to simulate the task condition (see below). When simulating the RS condition, $\beta = 0$.

The parameters $A$, $B$, $a$ and $b$ were selected to produce IPSPs longer in amplitude and latency in comparison with the EPSPs. The inverse of the characteristic time constant for the long-range EPSPs was defined as $\bar{a} = 0.5a$. This choice was based on the fact that long-range excitatory inputs onto pyramidal neurons target their apical dendrites, and consequently this slows down the time course of the EPSPs at the soma [50].

The input from brain areas $j \neq i$ to the region $i$ is given by

$$z_i(t) = \sum_{j=1, j\neq i}^{n} M_{ij} x_{3,j}(t) \tag{5}$$

The average PSP of pyramidal neurons in region $i$ characterizes the EEG-like signal in the source space; it is computed as [34, 44]

$$\nu(t)_i = C_2 x_{1,i}(t) - C_4 x_{2,i}(t) + C\alpha z_i(t) \tag{6}$$

The firing rates of pyramidal neurons $\zeta_i(t) = S(\nu(t)_i, r_0)$ were used to simulate the fMRI BOLD-like signals.

### 2.7 Simulations

We ran simulations to generate the equivalent of 21 min real-time recordings, discarding the first 60 s. The system of stochastic differential equations (4) was solved with the Euler–Maruyama method, using an integration step of 1 ms. We used 100 random seeds which controlled the stochasticity of the simulations. All the simulations were implemented in Python and the codes are freely available at `https://github.com/vandal-uv/Nicotine-Whole-Brain.git`.

### 2.8 Simulated fMRI-BOLD signals

We used the firing rates $\zeta_i(t)$ to simulate BOLD-like signals using a generalized hemodynamic model presented in [35]. In this model, an increment in the firing rate $\zeta_i(t)$ triggers a vasodilatory response $s_i$, producing blood inflow $f_i$, changes in the blood

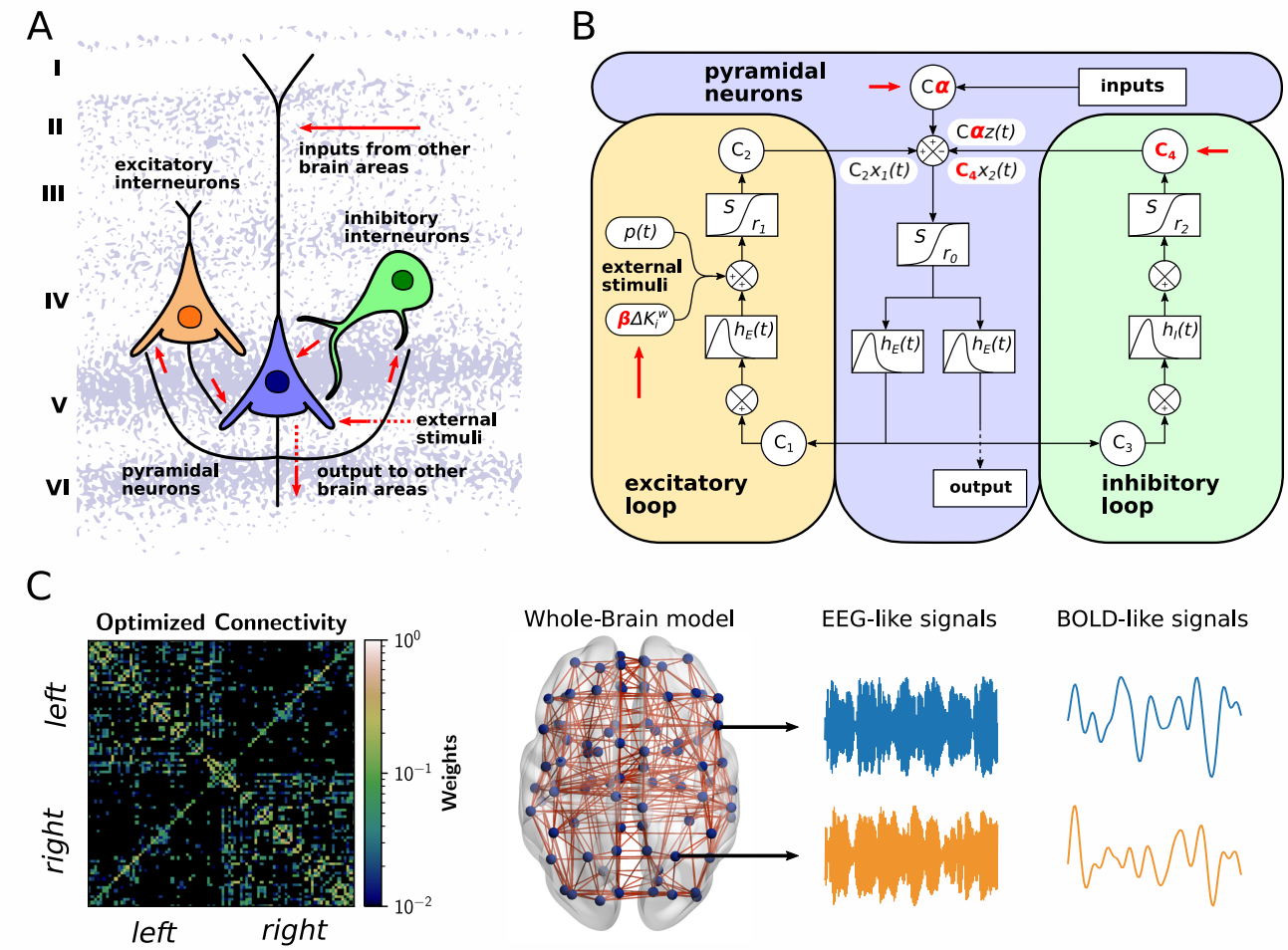


**Figure 1. Model for whole-brain dynamics. A)** Simplified scheme of the Jansen & Rit model, composed of a population of pyramidal neurons with excitatory and inhibitory local feedback mediated by interneurons. **B)** Overview of some important model parameters. Constants $C_i$ connect each population. The outputs are transformed from average pulse density to average postsynaptic membrane potential by an excitatory (inhibitory) impulse response function $h_E(t)$ ($h_I(t)$). A sigmoid function $S$ performs the inverse operation. Pyramidal neurons project to distant brain areas and receive both uncorrelated Gaussian-distributed inputs $p(t)$ and inputs from other regions $z(t)$, scaled by a global coupling parameter $\alpha$. For simulating the task, a term $\Delta K_i^w$ heterogeneously modifies the background input $p(t)$ to pyramidal neurons. **C)** Each node represents a brain region, whose dynamics are ruled by the Jansen & Rit equations. The optimized connectivity matrix is the map of the connections (and their weight in the color bar) between brain regions (row and columns of the matrix). This matrix was generated starting from the original human SC matrix. For each region, the model produces both EEG-like and BOLD-like signals. The brain figure in C) was obtained using the BrainNet Viewer [48]. The background figure in A) was adapted from [49] with permission.

volume $v_i$ and deoxyhemoglobin content $q_i$. The corresponding system of differential equations is

$$\begin{aligned}
\dot{s}_i(t) &= \zeta_i(t) - \frac{s_i(t)}{\tau_s} - \frac{f_i(t)-1}{\tau_f} \\
\dot{f}_i(t) &= s_i(t) \\
\dot{v}_i(t) &= \frac{f_i(t) - v_i(t)^{1/\kappa}}{\tau_v} \\
\dot{q}_i(t) &= \frac{\frac{f_i(t)(1-(1-E_0)^{1/f_i(t)})}{E_0} - \frac{q_i(t)v_i(t)^{1/\kappa}}{v_i(t)}}{\tau_q}
\end{aligned} \tag{7}$$

where $\tau_s = 0.65$, $\tau_f = 0.41$, $\tau_v = 0.98$, $\tau_q = 0.98$ represent the time constants for the signal decay, blood inflow, blood volume and deoxyhemoglobin content, respectively. The stiffness constant (resistance of the veins to blood flow) is given by $\kappa$, and the resting-state oxygen extraction rate by $E_0$. We used $\kappa = 0.32$, $E_0 = 0.4$. The BOLD-like signal of node $i$, denoted $B_i(t)$, is a non-linear function of $q_i(t)$ and $v_i(t)$

$$B_i(t) = V_0 \left[ k_1 \left(1 - q_i(t)\right) + k_2 \left(1 - \frac{q_i(t)}{v_i(t)}\right) + k_3 \left(1 - v_i(t)\right) \right], \tag{8}$$

where $V_0 = 0.04$ represents the fraction of venous blood (deoxygenated) in resting-state, and $k_1 = 2.77$, $k_2 = 0.2$, $k_3 = 0.5$ are kinetic constants.

The system of differential equations (7) was solved using the Euler method with an integration step of 10 ms. These BOLD-like signals were downsampled to the same sampling rate of empirical signals. Then, simulated signals were band-pass filtered between 0.01 and 0.1 Hz with a 3rd order Bessel filter. These BOLD-like signals were used to build the (FC) matrices –using pairwise Pearson correlations– from which the subsequent analysis of functional network properties was performed.

### 2.9 Nicotine and task modeling

To simulate the effects of nicotine, we decreased the value of the global coupling $\alpha$ and, consequently, the inhibitory-to-pyramidal neurons connectivity constant $C_4$. This mimics the effect, in a simple way, of nicotinic and muscarinic acetylcholine receptors on long-range connectivity [18, 20, 21] and feedback inhibition [22, 23, 51]. For simulating the task condition, we increase the factor $\beta$. This increases the mean background input that arrives at brain regions, in a manner that depends on the entries of $\Delta K_i^w$, the average empirical difference between the nodal FC strength in the RS and task blocks (placebo condition). The nodes that decrease their nodal strength the most, increment their background input the most [52].

### 2.10 Model fitting

We used the averaged empirical FC matrices across subjects as "targets" for model fitting. From the simulated BOLD-like signals, we built the simulated FC matrices with pairwise Pearson correlation. We vectorized the upper triangular of the empirical and simulated FC matrices, and then the vectors were compared using the euclidean distance. A lower distance value corresponds to a better fit.

Before fitting the model to the empirical fMRI data, we performed an optimization procedure over the human SC matrix $M$ [53]. We swept the parameter $\alpha \in [0.55, 0.89]$, and chose the value of alpha that minimized the euclidean distance of the empirical FC matrix in the placebo - RS block. This yielded $\alpha = 0.651$ for an euclidean distance and correlation, between matrices, around 0.15 and 0.3, respectively. From this point, we updated the values of the matrix $M$ iteratively –discarding negative entries– as following

$$M_{ij} = M_{ij} + \varepsilon \left( FC_{ij}^{emp} - FC_{ij}^{sim} \right) \tag{9}$$

with $FC_{ij}^{emp}$ as the empirical FC matrix in the placebo - RS block, $FC_{ij}^{sim}$ the simulated FC matrix at $\alpha = 0.651$, and $\varepsilon = 0.01$ the rate of convergence. We used 20 random seeds in each iteration, and computed an averaged FC matrix across random seeds. The results of the optimization are presented in the Fig. S4, where the euclidean distance decrease and correlation increase across iterations, indicating an improvement of the fitting. We employed this *optimized SC* matrix in the subsequent simulations, and it was not further changed. The codes for SC optimization can be found in https://github.com/vandal-uv/Nicotine-Whole-Brain.git.

To fit the model to the placebo and nicotine conditions - RS block, we swept $\alpha \in [0.6, 0.7]$ in steps of 0.001 and searched for the minimum distance between FCs. Using the value of the placebo - RS block ($\alpha = 0.648$), we swept the input slope $\beta \in [-0.5, 2.5]$ in steps of 0.03 for fitting the model to the placebo condition - task block. Then, employing $\beta = 0.58$ we swept $\alpha \in [0.6, 0.7]$ to fit the model to the nicotine condition - task block.

### 2.11 PET maps

We informed the model with acetylcholine-related receptors maps obtained by PET [36–41]. Specifically, we used the nicotinic $\alpha_4\beta_2$ receptor density map into AAL90 parcellation. Also, we compared the original map with random and uniform versions of the former. Starting from the placebo condition ($\alpha = 0.648$), we changed the $\alpha$ and $C_4$ parameters linearly with the density vector of the $\alpha_4\beta_2$ receptor maps, which was normalized between 0 and 1 dividing the vector by its maximal value. Thus, we now have a different value of the global coupling, and also local feedback inhibition, for each node

$$\begin{aligned} \alpha_i &= 0.648 + \Delta\alpha\lambda_i \\ C_{4,i} &= (0.3 + 0.6\alpha_i)C \end{aligned} \tag{10}$$

with $\Delta\alpha$ as the increment in the regional $\alpha_i$ parameter, and $\lambda_i$ the regional nodal value for the $\alpha_4\beta_2$ receptor density vector. We obtained convex curves similar to the observed in the Fig. 3. A narrow range of $\Delta\alpha$ values were employed: $\Delta\alpha \in [-0.012, 0.010]$ in steps of 0.0003. We calculated the minimal euclidean distance of the curves, and compared the values for each one of the maps employed. Before computing the minimal euclidean distance, we performed a polynomial regression (second-degree polynomial) on the $\Delta\alpha$ *vs.* distance curve in order to smooth the data, and then calculated the minimal distance from the fitted curves.

### 2.12 Functional integration and segregation

Starting from the FC matrices, we first applied a proportional threshold to remove spurious connectivity values [54]. Then, FC matrices were binarized and graph measures were computed. Specifically, we calculated the binary global efficiency and transitivity, metrics related integration and segregation, respectively [33].

Global efficiency is based in paths, and was defined as [55]

$$E = \frac{1}{n}\sum_{i}^{n} E_i = \frac{1}{n}\sum_{i}^{n} \frac{\sum_{j\neq i}^{n} d_{ij}^{-1}}{n-1} \tag{11}$$

with $E_i$ as the nodal efficiency, $n = 90$ the total number of nodes, and $d_{ij}$ the shortest path that connect two nodes $ij$. The global efficiency is bounded between 0 and 1. Higher values are expected to be found in very integrated networks, where nodes can easily reach each other; values near 0 means the opposite. Transitivity is based in the count of the triangular motifs of the network, and it was computed as [56]

$$T = \frac{\sum_{i}^{n} 2t_i}{\sum_{i}^{n} k_i(k_i-1)} \tag{12}$$

where $t_i$ corresponds to number of triangles around the node $i$, and $k_i$ the node degree. The first one is defined as

$$t_i = \frac{1}{2}\sum_{j\neq i}^{n}\sum_{h\neq j, h\neq i}^{n} a_{ij}a_{ih}a_{jh} \tag{13}$$

with $a_{ij} = 1$ if two nodes $ij$ are connected in the graph, and 0 otherwise. Transitivity captures the degree of local (short range) interactions between nodes and, in more common words, counts "in what extent my friends are also friends between them". Higher values are expected from segregated networks, and 0 the opposite (e.g., completely random networks).

To avoid the arbitrariness of choosing a single proportional threshold, we used a range of thresholds from 5 to 20% with linear increments of 1%. We report the area under the curve (AUC) of each graph metric in the threshold range explored [57]. Another issue regarding to network analysis in FC is related to the influence of overall FC (the strength of the FC matrix) on functional network topology [54]. To divorce the effect of overall FC from topology, we regressed out the overall FC from each graph metric as suggested by [54]. Regression was done combining the subjects (or seeds) in all conditions (placebo and nicotine in both RS and task). The slope was used to regress out the overall FC, and finally we reported the corrected graph metrics.

The graph analysis was performed using the Brain Connectivity Toolbox for Python (`https://github.com/fiuneuro/brainconn`) [33].

### 2.13 Statistical analysis

All pairwise comparisons, such as overall FC and and network metrics, were performed with nonparametric permutation tests. These tests are suitable when using small sample sizes, and do not require any assumptions about normality [58]. The real difference between groups (computed as the mean difference) was compared with the distribution obtained from 10000 random surrogates; they were acquired by randomly reassigning the measures between groups (e.g., placebo and nicotine). We reported the $p$ values, and results were considered as statistically significant for $p$ values $< 0.05$. In addition, statistical relationships were measured using Pearson and Spearman correlations.

## 3 Results

### 3.1 Effects of nicotine on functional network topology are context-dependent

We first analyzed the empirical fMRI data [32], under the hypotheses that 1) nicotine promotes functional segregation, and 2) the effects are context-dependent. Recordings were taken from 18 healthy smokers in two different conditions: placebo, or under the effects of nicotine in the form of a 4 mg nicotine polacrilex gum (Nicorette; McNeil AB). Brain areas were defined using the AAL90 anatomical parcellation, which reduces the brain to 90 cortical and subcortical regions [43]. BOLD-fMRI

was measured in RS and during a Go/No-Go attentional task and our main focus of attention is the functional brain networks captured by the FC matrix. Within the current analysis, we center our attention on the fMRI and behavioral data of first RS and task periods to avoid fatigue effects (see below).

The main effect of nicotine was to decrease the mean values within the FC matrices (named overall FC, Fig. 2A), the effect being stronger in the task block than in RS. Statistically significant differences in overall FC were found for task ($p = 0.0409$), but not for RS ($p = 0.1961$). Then, the FC matrices were assessed for functional integration and segregation, as described in Methods. Segregation was measured by the transitivity $T$, which is based on counting the network triangular motifs; a higher value is related to a network with highly interconnected local neighbors [33]. Integration was quantified by the global efficiency $E$, which depends on shortest paths; higher values are expected for networks with nodes that can easily reach each other [33]. As overall FC has an effect on the thresholded FC network topology [54], we regressed out the overall FC from graph metrics with a simple linear regression (Fig. S1). Throughout this work, we report the corrected graph metrics.

Nicotine produces an increase of $E$ (integration) in RS, and a decrease during task (Fig. 2A). However, results were not statistically significant for either condition ($p = 0.4188$ and 0.1985, respectively). On the contrary, nicotine increases $T$ (segregation), being this effect significant for the task block ($p = 0.0251$), but not for RS ($p = 0.3372$) (Fig. 2A). The results suggest that nicotine has a pro-segregation effect on the functional brain network topology, explained by the decrease in both overall FC and $E$ and the increase in $T$. However, these effects were observed only in the task block, pointing out the context-dependent nature of nicotine modulation.

To characterized, in a more local level, the effects of nicotine on task functional network topology, we computed nodal measures of segregation and integration: nodal clustering coefficient and nodal efficiency. Also, we grouped the brain regions in the commonly known RS networks [59]. We found a trend of nicotine, during task, of increasing the mean clustering coefficient of nodes that belongs to the extrastriate network ($p = 0.0791$), and a decrease in nodal clustering of sensorimotor network's nodes ($p < 0.0180$). No differences were found for nodal efficiency in any of the six RS networks considered.

To emphasize the context-dependent effect of nicotine, we repeated the network analysis on the three additional RS periods published in [32]. The first period is the one in Fig. 2A. The remaining periods were analyzed to explore the effect of fatigue on FC: time-on-task increases from RS period 1 to 4 (Fig. S2). Nicotine prevented the increase in overall FC triggered by time-on-task. Also, the increase of $E$ and decrease of $T$ caused by nicotine were more pronounced in RS periods 2 to 4, compared to period 1. Thus, in conditions of prolonged time-on-task, nicotine brakes the changes in RS FC triggered by tiredness [32]. However, for the remaining analysis we will only include the first RS and task periods, because considering the effects of fatigue in our computational model falls beyond the scope of our work.

Next, to find a link between functional network topology and behavior (task performance), we analyzed the reaction time (RT) of the Go trials, the errors (percentage of incorrect responses) of the No-Go trials, and the metrics computed from the FC matrices in the task block. As previously reported [32], the main effect of nicotine was to decrease the RT of the subjects during task ($p = 0.0037$) (Fig. 2B). Thus, subjects performed better under the effects of nicotine: a reduction in RT is a signature of enhanced attention [60]. When the RT is correlated with FC network metrics, we only found a significant negative correlation with the transitivity $T$ ($p = 0.0047$), finding no correlation with the overall FC ($p = 0.2070$) and a positive but non-significant correlation with $E$ ($p = 0.0971$) (Fig. 2B). Regarding the error rate (Fig. 2C), there is a trend of nicotine to reduce the percentage of incorrect responses, but the result was not significant ($p = 0.3208$). Also, we did not find a correlation between RT with overall FC ($p = 0.3145$), $E$ ($p = 0.1979$) and $T$ ($p = 0.1655$). Thus, subjects that increase their segregation (transitivity) the most, also decrease their RT. From the results it can be inferred that 1) a segregated network is suitable for the task (Go/No-Go), and 2) nicotine improves the reaction time of the subjects promoting a more segregated functional network during task.

Finally, to verify if the effects of the functional network topology on performance are specific of the task, we repeated the previous analysis using the metrics of the RS block (Fig. S3). We did not find a correlation between RT and errors with neither overall FC, $E$, nor $T$ ($p > 0.3807$ for all cases). Thus, RS metrics cannot predict the outcomes of the subjects in our Go/No-Go attentional task.

### 3.2 Modeling the effects of nicotine on functional connectivity

To suggest biophysical mechanisms for the effects of nicotine on functional network topology, we simulated the whole-brain dynamics using the Jansen & Rit neural mass model [34]. As with the experimental data, brain areas were defined using the AAL90 anatomical parcellation, and connected with a SC matrix derived from MRI [45]. The model was also informed with the empirical fMRI BOLD signals [32] (see below).

The Jansen & Rit model is built from three populations of neurons: pyramidal neurons, excitatory interneurons and inhibitory interneurons (Fig. 1A-B), contained in each brain region. To connect brain regions, we used a weighted, undirected optimized SC matrix, that was obtained Fig. 1C using an iterative optimization [53] of the original SC matrix used in [45] (Fig. S4). As long-range projections are mainly excitatory [46, 47], brain regions in the model are connected through pyramidal

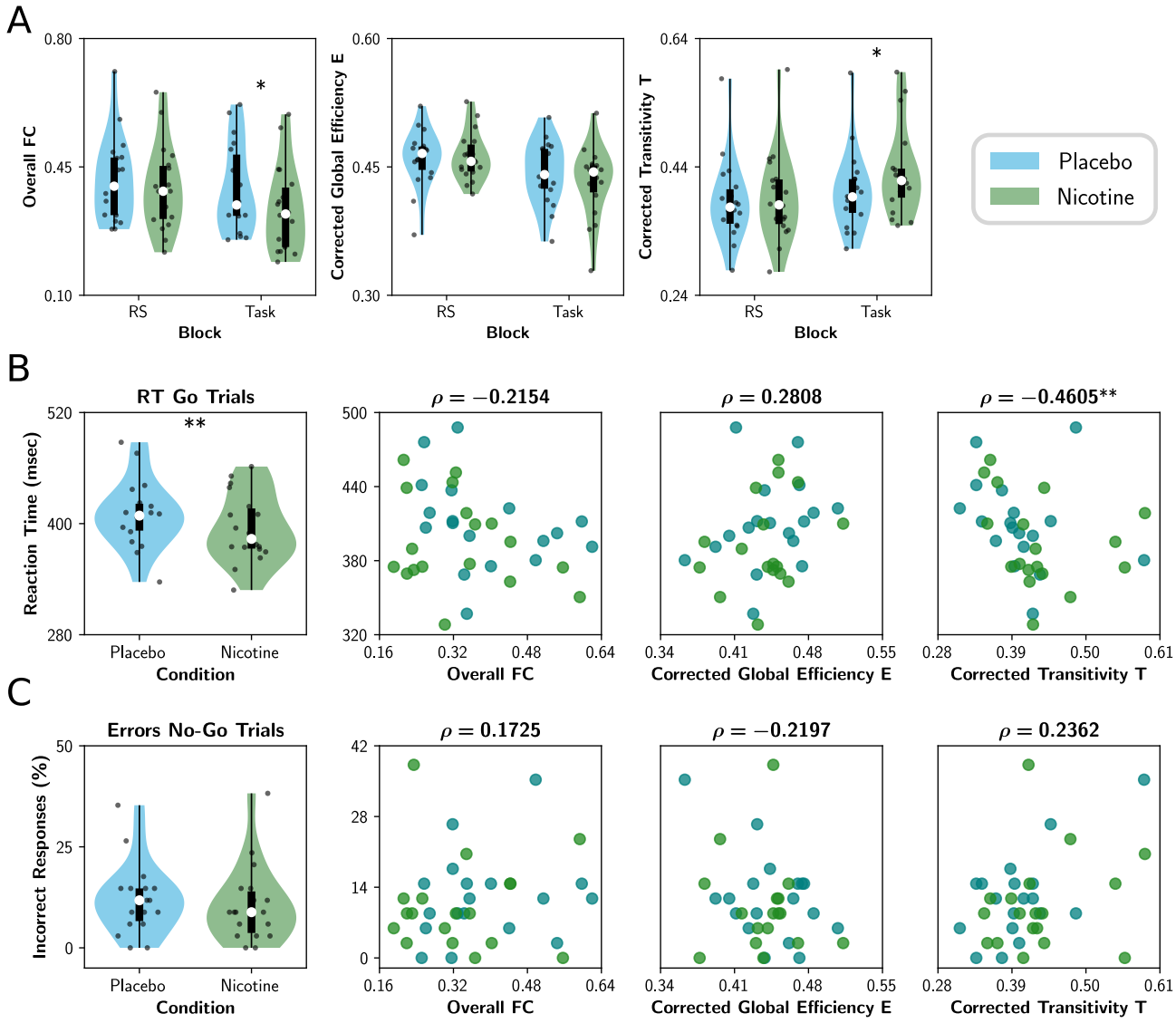


**Figure 2. Empirical changes in functional connectivity produced by nicotine. A)** Effect of nicotine on FC and functional network topology, both in RS and task. Violin plots represent the distributions of points (18 subjects per condition); the box plots represent the median (white circle), the first and third quartiles (box limits), and sample range (whiskers). **B)** Reaction time (RT) of the Go trials (left) and its correlation with FC metrics during the task. **C)** Percentage of incorrect responses of the No-Go trials (left) and correlation with FC metrics during task. Spearman $\rho$ was used as correlation measure. Points corresponded to participants (18 subjects per condition). ** : $p < 0.01$, * : $p < 0.05$.

populations. The simulations generate firing rates in each node of the network, which are used as an input to a generalized hemodynamic model [35] to generate BOLD-like signals (Fig. 1C) from which we built the FC matrices. We compared the empirical (averaged across subjects) and simulated FC matrices using the euclidean distance between the vectorized FCs; a lower value of distance is equivalent to a better fit.

The fitting steps are presented in Fig. 3A. First, using $\beta = 0$ (no task input) the model was fitted to RS, sweeping the global coupling $\alpha$ and comparing the simulated FC to an average of placebo and nicotine RS FCs. The comparison was made with the euclidean distance between matrices, and we found a minimum at $\alpha = 0.648$, for placebo, and at $\alpha = 0.644$, for nicotine (Fig. 3B). This confirms our previous hypothesis that a decrease in $\alpha$ and $C_4$ can be used to mimic the effects of nicotine. Next, to simulate the effect of the placebo condition - task block, we swept the input slope $\beta$ (Fig. 3C), finding a minimum at $\beta = 0.58$. A higher value of $\beta$, in general, represents an increase in the background input for almost all nodes, consistent with the idea that nodes that changed mostly their FC nodal strength, also increased its background input largely as an effect of the task

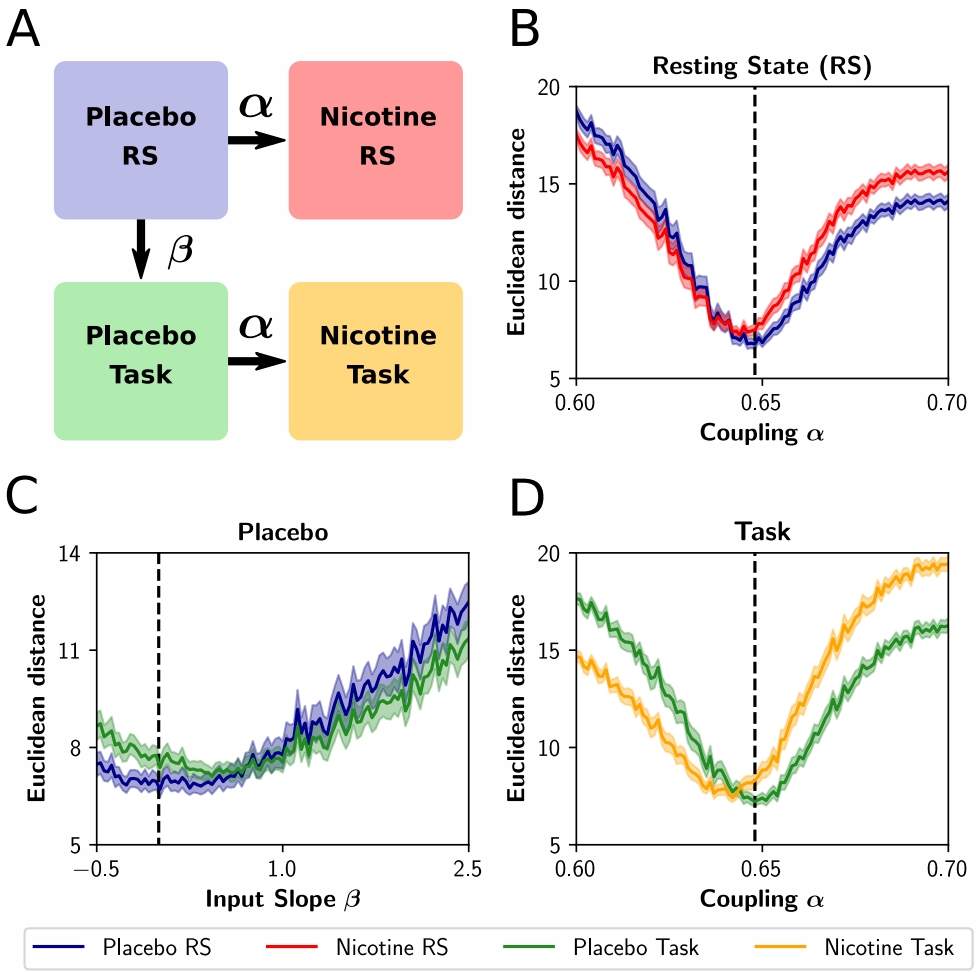


**Figure 3. Fitting the whole-brain model**. **A)** Starting from the model fitted to the placebo condition in RS (blue), the model was fit to the nicotine condition in RS sweeping the the parameter $\alpha$ (red). The fit to the placebo condition during task was performed by increasing $\beta$ (green). Finally, Using the $\beta$ value for placebo-task, the model was fit to nicotine-task by sweeping $\alpha$ (yellow). **B-D)** Euclidean distance between simulated and empirical FCs as a function of $\alpha$ and $\beta$. The minima of the Euclidean distances between empirical and simulated FC represent the values of the parameters $\alpha$ and $\beta$ that better reproduce the empirical FCs. Segmented lines correspond to the optimal values found for placebo-RS (B and C) and placebo-task (D). A decrease in $\alpha$ was accompanied by a decrease in $C_4$ (see text). Shaded areas represent the 95% confidence interval (using 100 random seeds).

[52]. Finally, using $\beta = 0.58$ we fitted the model to the nicotine condition - task block, sweeping $\alpha$ and finding a minimum at $\alpha = 0.641$. Thus, a larger decrease in global coupling and feedback inhibition is required to simulate the effects of nicotine during task.

Using the model with the fitted values of $\alpha$, $C_4$ and $\beta$, we obtained 100 simulated FCs (with different random seeds) for all four conditions (Fig. 4). Qualitatively, the averaged empirical (Fig. 4A) and simulated (Fig. 4B) FC matrices show that both nicotine and task decrease global correlations. Applying the network measures to the simulated FCs, our model reproduced the empirical results. First, nicotine decreases the overall FC (Fig. 4C) in both RS ($p = 410^{-5}$) and the task blocks ($p = 110^{-12}$), being the effect stronger in the latter. Similar to the empirical data, the following networks metrics were corrected for overall FC (Fig. S4). Second, nicotine reduces $E$ in task ($p = p = 110^{-12}$) (Fig. 4C), but not in RS ($p = 0.4325$). Lastly, nicotine increases $T$ (Fig. 4C) and the effect was stronger and significant in the task block ($p = 110^{-5}$) but not in RS ($p = 0.2738$). Thus, both simulated and empirical data suggest that nicotine has a pro-segregation effect on network topology only in the task block.

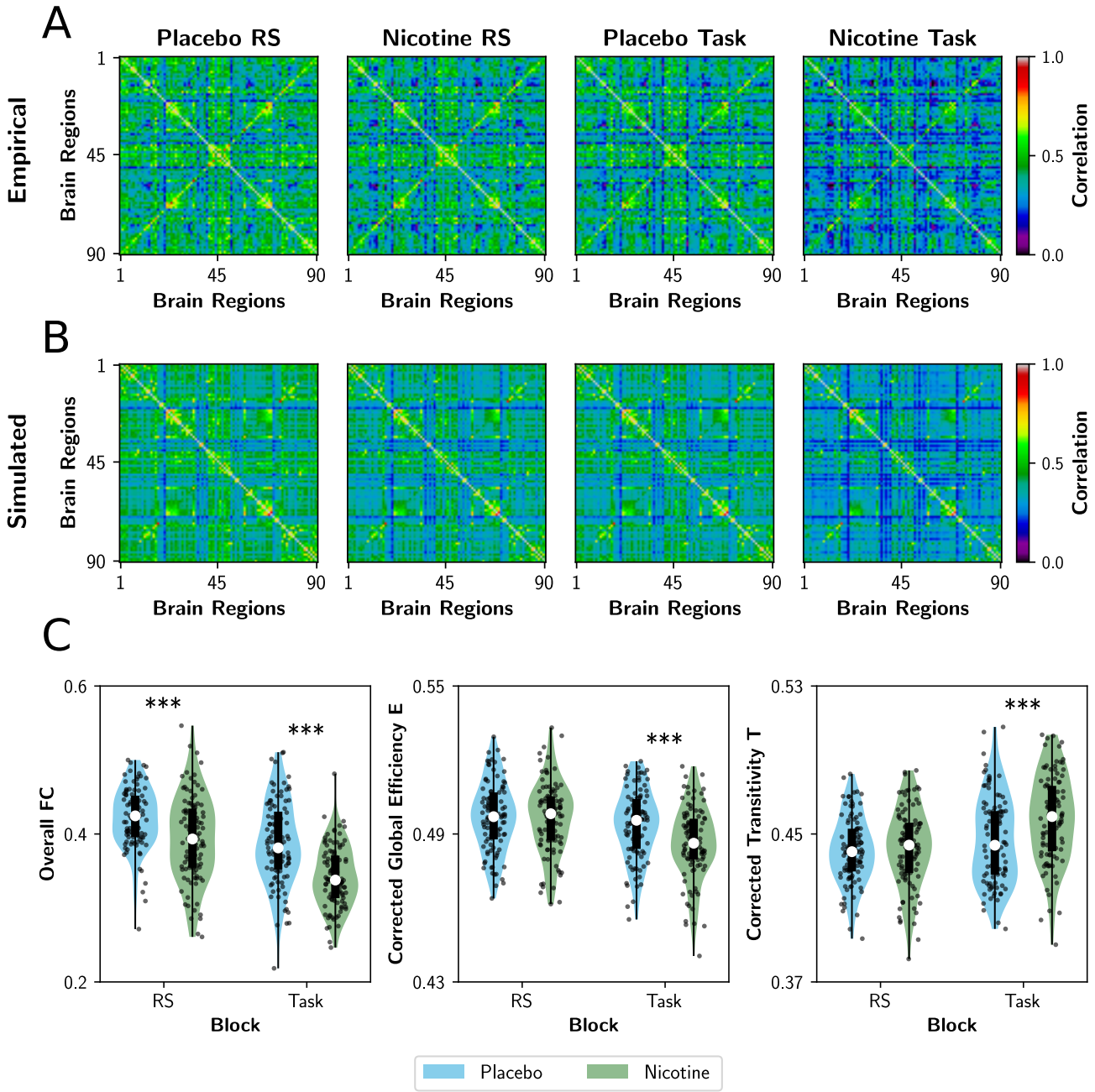


**Figure 4. Simulated changes in functional connectivity produced by nicotine.**. **A)** Empirical and **B)** simulated FC matrices, for all four conditions. For the empirical data, we show the average matrices across subjects ($n = 18$), and for the simulated data we show the average using different random seeds ($n = 100$). **C)** Simulated effects of nicotine on FC and network topology, both in RS and task. Violin plot represents the distributions of points (100 random seeds per condition); the box plot is constituted by the median (white circle), the first and third quartiles (box limits), and sample range (whiskers). *** : $p < 0.001$.

### 3.3 Nicotinic receptors partially mediate the changes in functional connectivity

Computational models suggest that the regional density of neurotransmitter receptors is a key element to precisely reproduce the changes in brain dynamics by neuromodulation [45, 61]. To assess this possibility, we tested if the regional density of cholinergic-related receptors can explain the effects of nicotine on FC. We used regional density maps, obtained with PET [36–41], to test what acetylcholine-related receptors are associated with the changes in FC observed in the empirical data. Specifically, we considered density maps –parcellated using AAL90– for the $\alpha_4\beta_2$ nicotinic receptor, the $M_1$ muscarinic

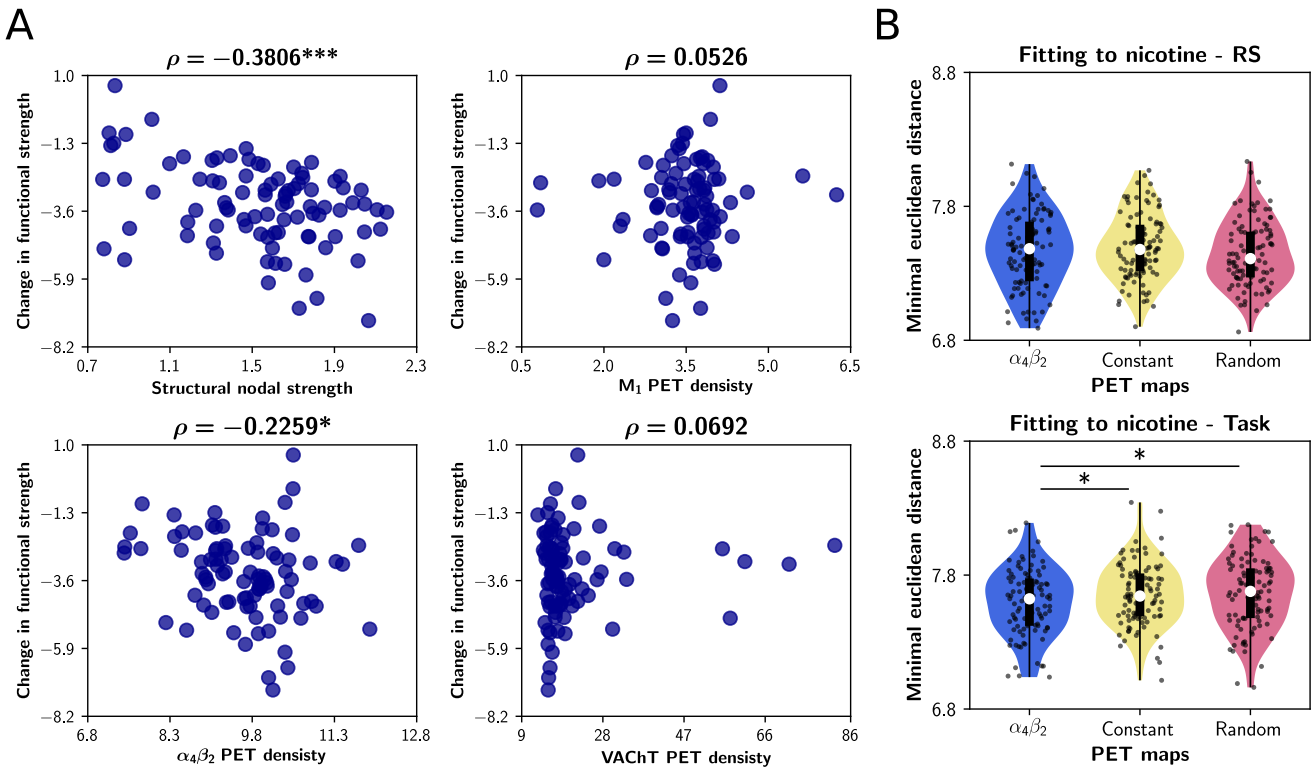


**Figure 5. Relationship between cholinergic receptors and the nicotine-mediated effects on FC. A)** Correlation between the change in empirical FC nodal strength (averaged for RS and task) with SC nodal strength and PET density of cholinergic-related receptors and transporters. **B)** Fitting to nicotine condition, both RS and task blocks, using the $\alpha_4\beta_2$ receptor density map. We compared the fitting of the original map with two different surrogates (random and uniform maps derived from the original $\alpha_4\beta_2$ receptor density vector). The minimal euclidean distance is shown. Violin plot represents the distributions of points (100 random seeds per condition); the box plot is constituted by the median (white circle), the first and third quartiles (box limits), and sample range (whiskers). Points corresponded to the AAL90 brain regions. * : $p < 0.05$, *** : $p < 0.001$.

receptor, and the vesicular acetylcholine transporter (VAChT). We calculated the difference in the empirical FC nodal strength between nicotine and placebo conditions (averaged across subjects and blocks), and correlated this vector with the density maps. In addition, we tested if the nodal strength of the optimized SC –a topological measure not related to receptors' density– correlates with the effects of nicotine on the FC.

Fig. 5 shows the correlation of SC nodal strength and density maps with the changes in FC nodal strength. First, we found a negative correlation between SC nodal strength and the change in FC ($p = 0.0002$, Fig. 5A). Thus, the nodes that are heavily connected in the network decrease most, by nicotine, their FC strength. On the side of receptors, we only found a modest negative correlation between the density of the $\alpha_4\beta_2$ receptor with the change in FC ($p = 0.0323$, Fig. 5A), but not for the $M_1$ receptor ($p = 0.6222$, Fig. 5A) and the VAChT ($p = 0.5170$, Fig. 5A). Thus, nodes expressing more $\alpha_4\beta_2$ receptor tend to show a greater reduction of their functional nodal strength. These results suggest that both the brain SC and the $\alpha_4\beta_2$ receptor might play a role in explaining the effects of nicotine on FC. To further validate the role of the $\alpha_4\beta_2$ receptor, we performed a multiple linear regression using the SC nodal strength and the $\alpha_4\beta_2$ density map as independent variables, and the change in FC as the dependent variable. We compared the two variables model (named SC + PET), with the simple linear regressions used before (SC and PET only). For each model, we calculated the Akaike information criterion (AIC) and found that the SC + PET model (using the $\alpha_4\beta_2$ receptor density data) was the best model (AIC = 302, $r^2$ = 0.1887), in comparison to the SC only (AIC = 306, $r^2$ = 0.1448) and the PET only models (AIC = 315, $r^2$ = 0.0510). Thus, both SC and nicotinic $\alpha_4\beta_2$ receptor density are key elements to explain the effects of nicotine on whole-brain FC.

If the $\alpha_4\beta_2$ receptor density correlates with the changes in FC, a model informed with the distribution of this receptor across the brain should improve the fitting to the empirical data. We analyzed this possibility repeating the fitting performed in Fig. 3 for the nicotine condition, both in RS and task blocks. However, this time we changed the parameters $\alpha$ and $C_4$ proportionally to the $\alpha_4\beta_2$ receptor density, starting from the placebo condition ($\alpha = 0.648$). Also, we used two different surrogates for

comparison purposes. They consisted in a randomization of the $\alpha_4\beta_2$ receptor density vector, and the uniform vector used in Fig. 3. We found that the $\alpha_4\beta_2$ receptor density map allows for a better fitting than the two surrogates maps, but only in the task block ($p = 0.0472$ and $p = 0.0238$ for uniform and random maps, respectively) and not in RS ($p = 0.2440$ and $p = 0.3151$, for uniform and random maps, respectively) Fig. 5B. Complementary, Cohen's d indicates a small effect size for $\alpha_4\beta_2$ receptor versus the constant and random surrogates ($d = -0.2431$ and $d = -0.2735$, respectively). Thus, the $\alpha_4\beta_2$ receptor could a play a key –but partial– role in explaining the effects of nicotine on whole-brain FC.

## 4 Discussion

We have explored the effects of nicotine on the brain's FC network topology analyzing fMRI data and computational modeling. Our main results support the hypothesis that cholinergic neuromodulation promotes functional segregation [4] in a context-dependent fashion: the effect is more pronounced when performing a task than during resting-state. In addition, functional segregation is correlated with in-task performance (reaction time), suggesting a link between FC network topology and behavior. Our computational modeling supports the idea that the global effects on the FC network are the result of well known local effects of acetylcholine: an increase in inhibition onto pyramidal neurons apical dendrites, alongside the decrease in somatic feedback inhibition. Finally, the correlation of both empirical and computational results with a map of $\alpha_4\beta_2$ receptor density, posit this receptor as an important factor determining the effects of nicotine. However, the same analysis reveals a more important role of a structural feature (structural nodal strengths) in determining the nicotine-induced changes in FC segregation.

When looking at the FC topology, the task promotes a more segregated functional network topology (see Fig. 2 and Fig. 4), and this increase in segregation is enhanced by the effects of nicotine. The stronger effect of nicotine on global correlations during task can have several explanations. If we expect that the task by itself promotes the release of endogenous acetylcholine [62], then nicotine could amplify the effect of cholinergic modulation by directly binding to nicotinic receptors or by promoting the release of more acetylcholine [63]. In our computational model, the heterogeneous increase in background input –to mimic the effects of the task– acts as a mechanism of network control [64], driving the network to a more functional segregated state without any change in the brain SC. From this point, nicotine produces a higher contrast with the placebo condition, reflected in the reduction of integration and increase in segregation observed with nicotine.

In our analysis, the degree of segregation correlates with in-task performance (Fig. 2B). In contrast, it has been well established that integration is associated with a better performance in a wide range of behavioral tasks [65]. However, segregation might be a convenient feature in relatively simpler, more monotonous or "automatic" motor tasks [65]. This was proposed by [3], arguing that simpler tasks requires the coordination of few brain subnetworks, and in this case a segregated network topology should be desirable for an optimal in-task performance. For example, enhanced segregation was reported in motor learning [66], visual-attentional [67] and sustained attention tasks [68]. In the specific case of [68], segregation increases in task-related networks (e.g. salience, cingulo-opercular, dorsal attention and visual networks), while integration jumps up in brain regions not involved in the task (auditory and sensorimotor networks). The increase in segregation might prevent the cross interference between brain networks, allowing the precisely processing of task-relevant information within the brain. In the other hand, the local increment of integration could constitute a mechanisms of top-down suppression, through network integration, of regions not relevant for the task [68]. The role of the cholinergic system in selectively decoupling brain regions, to process in a more efficient way external stimuli, is in accordance with the cholinergic shift to functional segregation during task [4].

Considering the effect of acetylcholine in enhancing attention in visual-spatial tasks [15, 18, 69], it is plausible to think that acetylcholine promotes segregation increasing the within and between network connectivity in regions involved in visual processing. We checked this possibility with a exploratory analysis, and measured the empirical change (nicotine - placebo, task block) in the nodal clustering coefficient, grouping also the brain regions in RS networks [59]. We found that nicotine increases (a trend without statistical significance) the mean nodal clustering coefficient of extrastriate network's nodes, and decreases the mean coefficient of sensorimotor network's nodes. That result is in line with the task-triggered increase in segregation reported by [68], where the increment in segregation was observed in regions involved in visual processing and attention. Furthermore, our results resonate with the work of [70]. A long-term entrainment in a visual-attentional task promotes changes in brain SC, changes that comprise an increase of within and between connectivity in occipital and parietal brain regions, both required for processing visual information. Topologically, they found an increase in local efficiency (segregation) within the occipito-parietal network. This case is interestingly because the morph in network topology, which also was non-transient (long-standing), might comprise plasticity changes in the SC that enhance the bandwith of communication between and within occipital and parietal regions [70]. The cholinergic system could play a similar role mediating transient changes in network topology, changes that facilitate the processing of visual information from noisy signals.

We found a negative correlation between the nicotinic $\alpha_4\beta_2$ receptor density, obtained by PET, and the change in FC nodal strength. In fact, this result should not be a surprise, considering that FC changes were analyzed under the effects of nicotine. Despite this, the result emphasizes that the changes observed in FC can be ascribed to the cholinergic system and,

more specifically, to nicotinic receptors. The nicotinic $\alpha_4\beta_2$ receptor has a prominent role in attention and cognition [17]. For example, a dysfunction in $\alpha_4\beta_2$ receptors is associated by cognitive impairments in mild Alzheimer dementia [71]. Also, stimulation of $\alpha_4\beta_2$ receptors enhances performance in visual attentional tasks [72, 73], while their selective inhibition produces the opposite results [72]. Incorporating the $\alpha_4\beta_2$ PET density map in the whole-brain model also improved the fit to the nicotine condition in the task block, but not in RS. This highlights the role of $\alpha_4\beta_2$ receptor in mediating the nicotine-induced changes in FC. However, it is important to remark that the effect of incorporating the map was small, and observed only in the task block. A possible explanation relies in the relatively low correlation between the $\alpha_4\beta_2$ density map with the changes in FC nodal strength (Fig. 5A), and/or the small effects of nicotine on FC in RS, compared to the task (Fig. 2A and Fig. 4C). On the other hand, the SC nodal strength correlates well with the difference in FC nodal strength. Therefore, the structural brain connectivity plays a pivotal role in setting the changes in FC by nicotine. There are some theoretical works arguing that the nodal properties, derived from the SC, better explain the effects of neuromodulation on brain dynamics [29, 74, 75]. In consequence, it is plausible to think that the interaction between SC, neuromodulatory systems (and their receptors) and FC is not straightforward.

The mechanisms employed here are compatible with previous computational models, which attempted to simulate the effects of acetylcholine on global brain dynamics [28, 30, 76]. In these works, a decrease in global coupling and spike-frequency adaptation has been proposed to simulate the influence of acetylcholine in the transition from sleep to wakefulness [30, 76]. A similar mechanism was proposed by [28], who simulated the effects of acetylcholine by increasing the neural gain (the slope of the input-output function of neural masses) and decreasing global coupling. The main difference in our model was the introduction of a reduced feedback inhibition as an effect of nicotine, in contrast to the increment in neural gain used in [28]. However, in all the aforementioned cases (including our work), the increase in segregation is compatible with the reduction in global coupling by the cholinergic system. Indeed, the mechanisms are in accordance with the shift from internal to external processing of information within the brain by acetylcholine [19], as a consequence of reducing the influence of feedback connections in relation to external stimulation.

Another interesting finding is the lack of correlation between overall FC and task performance as measured by the RT, and in parallel the negative correlation we found between segregation and RT. Although one of the main effects of nicotine in light of our results was to decrease the global correlations (overall FC), the change in network topology better predicted subjects' performance in the Go/No-Go task. Moreover, the topology of the FC network during the task was better at predicting performance during the task, in contrast to the topology of the FC network during RS. Thus, our findings suggest that 1) network topology matters for predicting performance during the task and 2) as pointed out by [28], a characterization of RS FC is not sufficient to explain the effects of neuromodulatory systems on behaviour. Following this idea, [9] reported a context-dependent effect of noradrenergic neuromodulation. The authors found an increase in RS segregation triggered by atomoxetine (a noradrenaline reuptake inhibitor). However, the opposite results were observed during an N-back task where Atomoxextin increases functional integration. They suggest that the cognitive load of the N-back task, compared with the lack of cognitive constraints at RS, enhances phasic firing patterns of the locus coeruleus, which in turn could be potentiated by atomoxetine and ultimately promote functional brain integration.

Based on this work, there is plenty of ideas to explore. For example, the mechanisms used here could be adapted to simulate the effects of the cholinergic system during the transition from sleep to wakefulness, similar to [30] and [76]. In addition, whole-brain models could be used to test specific targets for pharmacological treatments [45]. By combining fMRI, structural, and neurotransmitter PET data, personalised whole-brain models can be used to find specific targets for brain disorders. This could lead to new treatments for disorders in which the cholinergic system is impaired, such as Alzheimer's disease and age-related cognitive decline [77]. With a more theoretical motivation, we consider here only pairwise interactions and neglect higher-order effects that might contain relevant information related to high-dimensional functional brain interactions. Information theory [78] and algebraic topological approaches [79, 80] may provide useful information about high-order interdependencies in the brain. Indeed, a whole-brain model was proposed as a non-linear model of neurodegeneration to simulate the ageing of connectomes [81]. This model successfully reproduced the changes of high-order statistics observed in neuroimaging data [82], specifically, a significant increase in redundancy-dominated interdependencies between BOLD activity in older subjects. In this scenario, it would be interesting to reverse the ageing-triggered increment in redundancy by simulating the effect of cholinergic neuromodulation in a whole-brain model.

We must point out some limitations of our work. First, nicotine is not a full pro-cholinergic drug, as are donepezil, galantamine, and rivastigmine, which are cholinesterase inhibitors. However, nicotine may promote the release of acetylcholine [63], which is plausible given that nicotinic receptors are widely expressed in several types of neurons types, including cholinergic neurons [83]. Moreover, the decrease in global correlations by nicotine reported here was also observed under the effects of donepezil [28]. In view of these points, we believe that our generalization linking the influence of nicotine to the pro-segregation effects of the cholinergic system [4], constitutes a reasonable statement. A second limitation is that the empirical SC and the PET density maps, do not belong to the same subjects as the empirical fMRI recordings used in this work.

We partially solved this problem using SC optimization, similar to [53]. Moreover, the analysis performed here considers only the static FC, how FC and functional network topology change over time should be addressed in future [10, 29, 84].

### 4.1 Conclusions

Overall, our results suggest mechanisms to explain the pro-segregation effects of the cholinergic system, that are compatible with previous computational models and the biophysics of nicotine action. We observed that the pro-segregation effects of nicotine, at the whole-brain level, depends on the behavioral context that subjects are experiencing. Furthermore, the degree of in-task segregation, captured as network transitivity, correlates with behavioral performance in a visual-attentional task. We suggest that, in this specific scenario, network segregation might be suitable for optimal in-task performance (segregation reduces reaction time). Finally, we observed that the regional expression of the nicotinic $\alpha_4\beta_2$ receptor improves the fitting of the model to the empirical data, allowing the model to explain better the effect of nicotine during the task block. However, embodying PET density maps into the model has a marginal effects on the fit goodness, pointing out that other "actors", such as brain structural connectivity, might play a role mediating the effects of nicotine on whole-brain functional connectivity.

To our knowledge, this is the first work that combines empirical fMRI data, in-task performance, and computational modeling to study the effects of the cholinergic system on functional network topology. Establishing links between neuromodulation and its functional correlates has great scientific potential to deepen our understanding of the brain and its context-dependent response, and more generally to shed new light on the complex relationships between the structure and function of the human brain.

## Acknowledgements

We thank to Gustavo Deco for kindly providing the structural connectivity matrix used in the model. This work was supported by Fondecyt Grants 1211750 (PO) and 11181072 (RC), and the Advanced Center for Electrical and Electronic Engineering (FB0008 ANID, Chile). The Centro Interdisciplinario de Neurociencia de Valparaíso (CINV) is supported by ICM-ANID, Grant ACE210014. CC-O is funded by Beca Doctorado Nacional ANID 2018-21180995, and the Latin American Brain Health Institute (BrainLat). The analysed data derive from a study of [32] funded by Deutsche Forschungsgemeinschaft Grant GI 682/2-1 (CG).

## Author contributions statement

**Carlos Coronel-Oliveros:** Conceptualization, Investigation, Methodology, Formal analysis, Writing - original draft, Visualization, Validation. **Carsten Gießing:** Investigation, Data curation, Writing - review & editing, Supervision, Funding acquisition. **Vicente Medel:** Investigation, Methodology, Writing - review & editing. **Rodrigo Cofré:** Conceptualization, Investigation, Writing - review & editing, Methodology, Supervision. **Patricio Orio:** Conceptualization, Investigation, Writing - review & editing, Methodology, Supervision, Project administration, Resources.

## Competing interests statement

The authors declare that the research was conducted in the absence of any commercial or financial relationships that could be construed as a potential conflict of interest.

## Data availability statement

All the codes used to perform the simulations are freely available in the next github repository `https://github.com/vandal-uv/Nicotine-Whole-Brain`. The graph analysis was performed using the Brain Connectivity Toolbox for Python (`https://github.com/fiuneuro/brainconn`) [33]. Data are available on request from Dr. Carsten Gießing, University of Oldenburg (email: carsten.giessing@uni-oldenburg.de). A formal data sharing agreement is required.

## References

1. Dehaene, S. & Changeux, J. P. Experimental and Theoretical Approaches to Conscious Processing. *Neuron* DOI: https://doi.org/10.1016/j.neuron.2011.03.018 (2011).

2. Sporns, O. Network attributes for segregation and integration in the human brain. *Curr. opinion neurobiology* **23**, 162–171, DOI: https://doi.org/10.1016/j.conb.2012.11.015 (2013).

3. Cohen, J. R. & D'Esposito, M. The segregation and integration of distinct brain networks and their relationship to cognition. *J. Neurosci.* **36**, 12083–12094, DOI: https://doi.org/10.1523/JNEUROSCI.2965-15.2016 (2016).

4. Shine, J. M. Neuromodulatory influences on integration and segregation in the brain. *Trends cognitive sciences* DOI: https://doi.org/10.1016/j.tics.2019.04.002 (2019).

5. Kelso, J. S. Multistability and metastability: understanding dynamic coordination in the brain. *Philos. Transactions Royal Soc. B: Biol. Sci.* **367**, 906–918, DOI: https://doi.org/10.1098/rstb.2011.0351 (2012).

6. Tognoli, E. & Kelso, J. S. The metastable brain. *Neuron* **81**, 35–48, DOI: https://doi.org/10.1016/j.neuron.2013.12.022 (2014).

7. Bullmore, E. & Sporns, O. Complex brain networks: graph theoretical analysis of structural and functional systems. *Nat. reviews neuroscience* **10**, 186–198, DOI: https://doi.org/10.1038/nrn2575 (2009).

8. González, G. F. *et al.* Graph analysis of eeg resting state functional networks in dyslexic readers. *Clin. Neurophysiol.* **127**, 3165–3175, DOI: https://doi.org/10.1016/j.clinph.2016.06.023 (2016).

9. Shine, J. M., van den Brink, R. L., Hernaus, D., Nieuwenhuis, S. & Poldrack, R. A. Catecholaminergic manipulation alters dynamic network topology across cognitive states. *Netw. Neurosci.* **2**, 381–396, DOI: https://doi.org/10.1162/netn_a_00042 (2018).

10. Shine, J. M. *et al.* The dynamics of functional brain networks: integrated network states during cognitive task performance. *Neuron* **92**, 544–554, DOI: https://doi.org/10.1016/j.neuron.2016.09.018 (2016).

11. Wang, R. *et al.* Segregation, integration, and balance of large-scale resting brain networks configure different cognitive abilities. *Proc. Natl. Acad. Sci.* **118**, DOI: https://doi.org/10.1073/pnas.2022288118 (2021).

12. Hadley, J. A. *et al.* Change in brain network topology as a function of treatment response in schizophrenia: a longitudinal resting-state fmri study using graph theory. *npj Schizophr.* **2**, 1–7, DOI: https://doi.org/10.1038/npjschz.2016.14 (2016).

13. delEtoile, J. & Adeli, H. Graph theory and brain connectivity in alzheimer's disease. *The Neurosci.* **23**, 616–626, DOI: https://doi.org/10.1177/1073858417702621 (2017).

14. Chen, Y. *et al.* Disrupted brain functional networks in drug-naive children with attention deficit hyperactivity disorder assessed using graph theory analysis. *Hum. brain mapping* **40**, 4877–4887, DOI: https://doi.org/10.1002/hbm.24743 (2019).

15. Thiele, A. & Bellgrove, M. A. Neuromodulation of attention. *Neuron* **97**, 769–785, DOI: https://doi.org/10.1016/j.neuron.2018.01.008 (2018).

16. Shine, J. M. *et al.* Computational models link cellular mechanisms of neuromodulation to large-scale neural dynamics. *Nat. neuroscience* **24**, 765–776, DOI: https://doi.org/10.1038/s41593-021-00824-6 (2021).

17. Hasselmo, M. E. & Sarter, M. Modes and models of forebrain cholinergic neuromodulation of cognition. *Neuropsychopharmacology* **36**, 52–73, DOI: https://doi.org/10.1038/npp.2010.104 (2011).

18. Picciotto, M. R., Higley, M. J. & Mineur, Y. S. Acetylcholine as a neuromodulator: cholinergic signaling shapes nervous system function and behavior. *Neuron* **76**, 116–129, DOI: https://doi.org/10.1016/j.neuron.2012.08.036 (2012).

19. Honey, C. J., Newman, E. L. & Schapiro, A. C. Switching between internal and external modes: a multiscale learning principle. *Netw. Neurosci.* **1**, 339–356, DOI: https://doi.org/10.1162/NETN_a_00024 (2017).

20. Kimura, F. Cholinergic modulation of cortical function: a hypothetical role in shifting the dynamics in cortical network. *Neurosci. research* **38**, 19–26, DOI: https://doi.org/10.1016/S0168-0102(00)00151-6 (2000).

21. Poorthuis, R. B. *et al.* Layer-specific modulation of the prefrontal cortex by nicotinic acetylcholine receptors. *Cereb. cortex* **23**, 148–161, DOI: https://doi.org/10.1093/cercor/bhr390 (2013).

22. Kruglikov, I. & Rudy, B. Perisomatic gaba release and thalamocortical integration onto neocortical excitatory cells are regulated by neuromodulators. *Neuron* **58**, 911–924, DOI: https://doi.org/10.1016/j.neuron.2008.04.024 (2008).

23. Askew, C. E., Lopez, A. J., Wood, M. A. & Metherate, R. Nicotine excites vip interneurons to disinhibit pyramidal neurons in auditory cortex. *Synapse* **73**, e22116, DOI: https://doi.org/10.1002/syn.22116 (2019).

**24.** Fino, E., Packer, A. M. & Yuste, R. The logic of inhibitory connectivity in the neocortex. *The Neurosci.* **19**, 228–237, DOI: https://doi.org/10.1177/1073858412456743 (2013).

**25.** Tremblay, R., Lee, S. & Rudy, B. Gabaergic interneurons in the neocortex: from cellular properties to circuits. *Neuron* **91**, 260–292, DOI: https://doi.org/10.1016/j.neuron.2016.06.033 (2016).

**26.** Poorthuis, R. B. & Mansvelder, H. D. Nicotinic acetylcholine receptors controlling attention: behavior, circuits and sensitivity to disruption by nicotine. *Biochem. pharmacology* **86**, 1089–1098, DOI: https://doi.org/10.1016/j.bcp.2013.07.003 (2013).

**27.** Coull, J. T., Büchel, C., Friston, K. J. & Frith, C. D. Noradrenergically mediated plasticity in a human attentional neuronal network. *Neuroimage* **10**, 705–715, DOI: https://doi.org/10.1006/nimg.1999.0513 (1999).

**28.** Pfeffer, T. *et al.* Circuit mechanisms for the chemical modulation of cortex-wide network interactions and behavioral variability. *Sci. Adv.* **7**, eabf5620, DOI: https://doi.org/10.1126/sciadv.abf5620 (2021).

**29.** Shine, J. M., Aburn, M. J., Breakspear, M. & Poldrack, R. A. The modulation of neural gain facilitates a transition between functional segregation and integration in the brain. *Elife* **7**, e31130, DOI: https://doi.org/10.7554/eLife.31130.001 (2018).

**30.** Deco, G., Hagmann, P., Hudetz, A. G. & Tononi, G. Modeling resting-state functional networks when the cortex falls asleep: local and global changes. *Cereb. cortex* **24**, 3180–3194, DOI: https://doi.org/10.1093/cercor/bht176 (2014).

**31.** Shine, J. M. *et al.* Human cognition involves the dynamic integration of neural activity and neuromodulatory systems. *Nat. neuroscience* **22**, 289–296, DOI: https://doi.org/10.1038/s41593-018-0312-0 (2019).

**32.** Gießing, C., Thiel, C. M., Alexander-Bloch, A. F., Patel, A. X. & Bullmore, E. T. Human brain functional network changes associated with enhanced and impaired attentional task performance. *J. Neurosci.* **33**, 5903–5914, DOI: https://doi.org/10.1523/JNEUROSCI.4854-12.2013 (2013).

**33.** Rubinov, M. & Sporns, O. Complex network measures of brain connectivity: uses and interpretations. *Neuroimage* **52**, 1059–1069, DOI: https://doi.org/10.1016/j.neuroimage.2009.10.003 (2010).

**34.** Jansen, B. H. & Rit, V. G. Electroencephalogram and visual evoked potential generation in a mathematical model of coupled cortical columns. *Biol. cybernetics* **73**, 357–366, DOI: https://doi.org/10.1007/bf00199471 (1995).

**35.** Stephan, K. E., Weiskopf, N., Drysdale, P. M., Robinson, P. A. & Friston, K. J. Comparing hemodynamic models with dcm. *Neuroimage* **38**, 387–401, DOI: https://doi.org/10.1016/j.neuroimage.2007.07.040 (2007).

**36.** Hillmer, A. T. *et al.* Imaging of cerebral $\alpha 4\beta 2^*$ nicotinic acetylcholine receptors with (-)-[18f] flubatine pet: Implementation of bolus plus constant infusion and sensitivity to acetylcholine in human brain. *Neuroimage* **141**, 71–80, DOI: https://doi.org/10.1016/j.neuroimage.2016.07.026 (2016).

**37.** Aghourian, M. *et al.* Quantification of brain cholinergic denervation in alzheimer's disease using pet imaging with [18 f]-feobv. *Mol. psychiatry* **22**, 1531–1538, DOI: https://doi.org/10.1038/mp.2017.183 (2017).

**38.** Baldassarri, S. R. *et al.* Use of electronic cigarettes leads to significant beta2-nicotinic acetylcholine receptor occupancy: evidence from a pet imaging study. *Nicotine Tob. Res.* **20**, 425–433, DOI: https://doi.org/10.1093/ntr/ntx091 (2018).

**39.** Bedard, M.-A. *et al.* Brain cholinergic alterations in idiopathic rem sleep behaviour disorder: a pet imaging study with 18f-feobv. *Sleep medicine* **58**, 35–41, DOI: https://doi.org/10.1016/j.sleep.2018.12.020 (2019).

**40.** Hansen, J. Y. *et al.* Mapping neurotransmitter systems to the structural and functional organization of the human neocortex. *bioRxiv* DOI: https://www.biorxiv.org/content/10.1101/2021.10.28.466336v2 (2021).

**41.** Naganawa, M. *et al.* First-in-human assessment of 11c-lsn3172176, an m1 muscarinic acetylcholine receptor pet radiotracer. *J. Nucl. Medicine* **62**, 553–560, DOI: https://doi.org/10.2967/jnumed.120.246967 (2021).

**42.** Conners, C. K. *The Conners Continuous Performance Test. Toronto: Multi-Health Systems* (Inc, 1994).

**43.** Tzourio-Mazoyer, N. *et al.* Automated anatomical labeling of activations in spm using a macroscopic anatomical parcellation of the mni mri single-subject brain. *Neuroimage* **15**, 273–289, DOI: https://doi.org/10.1006/nimg.2001.0978 (2002).

**44.** Jansen, B. H., Zouridakis, G. & Brandt, M. E. A neurophysiologically-based mathematical model of flash visual evoked potentials. *Biol. cybernetics* **68**, 275–283, DOI: https://doi.org/10.1007/BF00224863 (1993).

**45.** Deco, G. *et al.* Whole-brain multimodal neuroimaging model using serotonin receptor maps explains non-linear functional effects of lsd. *Curr. biology* **28**, 3065–3074, DOI: https://doi.org/10.1016/j.cub.2018.07.083 (2018).

**46.** Gilbert, C. D., Hirsch, J. A. & Wiesel, T. N. Lateral interactions in visual cortex. In *Cold Spring Harbor symposia on quantitative biology*, vol. 55, 663–677, DOI: https://doi.org/10.1101/SQB.1990.055.01.063 (Cold Spring Harbor Laboratory Press, 1990).

**47.** McGuire, B. A., Gilbert, C. D., Rivlin, P. K. & Wiesel, T. N. Targets of horizontal connections in macaque primary visual cortex. *J. Comp. Neurol.* **305**, 370–392, DOI: https://doi.org/10.1002/cne.903050303 (1991).

**48.** Xia, M., Wang, J. & He, Y. Brainnet viewer: a network visualization tool for human brain connectomics. *PloS one* **8**, e68910, DOI: https://doi.org/10.1371/journal.pone.0068910 (2013).

**49.** Schmolesky, M. The primary visual cortex. In Kolb, H., Nelson, R., Fernandez, E. & Jones, B. (eds.) *Webvision: The Organization of the Retina and Visual System* (Moran Eye Center, 2016).

**50.** Branco, T. & Häusser, M. Synaptic integration gradients in single cortical pyramidal cell dendrites. *Neuron* **69**, 885–892, DOI: https://doi.org/10.1016/j.neuron.2011.02.006 (2011).

**51.** Zerbi, V. *et al.* Rapid reconfiguration of the functional connectome after chemogenetic locus coeruleus activation. *Neuron* **103**, 702–718, DOI: https://doi.org/10.1016/j.neuron.2019.05.034 (2019).

**52.** Ito, T. *et al.* Task-evoked activity quenches neural correlations and variability across cortical areas. *PLoS computational biology* **16**, e1007983, DOI: https://doi.org/10.1371/journal.pcbi.1007983 (2020).

**53.** Deco, G. *et al.* Awakening: Predicting external stimulation to force transitions between different brain states. *Proc. Natl. Acad. Sci.* **116**, 18088–18097, DOI: https://doi.org/10.1073/pnas.1905534116 (2019).

**54.** van den Heuvel, M. P. *et al.* Proportional thresholding in resting-state fmri functional connectivity networks and consequences for patient-control connectome studies: Issues and recommendations. *Neuroimage* **152**, 437–449, DOI: https://doi.org/10.1016/j.neuroimage.2017.02.005 (2017).

**55.** Latora, V. & Marchiori, M. Efficient behavior of small-world networks. *Phys. review letters* **87**, 198701, DOI: https://doi.org/10.1103/PhysRevLett.87.198701 (2001).

**56.** Newman, M. The structure and function of complex networks. *SIAM review* **45**, 167–256, DOI: https://doi.org/10.1137/S003614450342480 (2003).

**57.** Ginestet, C. E., Nichols, T. E., Bullmore, E. T. & Simmons, A. Brain network analysis: separating cost from topology using cost-integration. *PloS one* **6**, e21570, DOI: https://doi.org/10.1371/journal.pone.0021570 (2011).

**58.** Nichols, T. E. & Holmes, A. P. Nonparametric permutation tests for functional neuroimaging: a primer with examples. *Hum. brain mapping* **15**, 1–25, DOI: https://doi.org/10.1002/hbm.1058 (2002).

**59.** Beckmann, C. F., DeLuca, M., Devlin, J. T. & Smith, S. M. Investigations into resting-state connectivity using independent component analysis. *Philos. Transactions Royal Soc. B: Biol. Sci.* **360**, 1001–1013, DOI: https://doi.org/10.1098/rstb.2005.1634 (2005).

**60.** Carlson, J. S., Jensen, C. M. & Widaman, K. F. Reaction time, intelligence, and attention. *Intelligence* **7**, 329–344, DOI: https://doi.org/10.1016/0160-2896(83)90008-9 (1983).

**61.** Luppi, A. I. *et al.* Paths to oblivion: Common neural mechanisms of anaesthesia and disorders of consciousness. *bioRxiv* DOI: https://www.biorxiv.org/content/10.1101/2021.02.14.431140v2 (2021).

**62.** Lohani, S. *et al.* Dual color mesoscopic imaging reveals spatiotemporally heterogeneous coordination of cholinergic and neocortical activity. *bioRxiv* DOI: https://www.biorxiv.org/content/10.1101/2020.12.09.418632v2 (2020).

**63.** Nordberg, A., Romanelli, L., Sundwall, A., Bianchi, C. & Beani, L. Effect of acute and subchronic nicotine treatment on cortical acetylcholine release and on nicotinic receptors in rats and guinea-pigs. *Br. journal pharmacology* **98**, 71–78, DOI: https://doi.org/10.1111/j.1476-5381.1989.tb16864.x (1989).

**64.** Gu, S. *et al.* Controllability of structural brain networks. *Nat. communications* **6**, 1–10, DOI: https://doi.org/10.1038/ncomms9414 (2015).

**65.** Shine, J. M. & Poldrack, R. A. Principles of dynamic network reconfiguration across diverse brain states. *NeuroImage* **180**, 396–405, DOI: https://doi.org/10.1016/j.neuroimage.2017.08.010 (2018).

**66.** Bassett, D. S., Yang, M., Wymbs, N. F. & Grafton, S. T. Learning-induced autonomy of sensorimotor systems. *Nat. neuroscience* **18**, 744–751, DOI: https://doi.org/10.1038/nn.3993 (2015).

**67.** Wang, R., Su, X., Chang, Z., Lin, P. & Wu, Y. Flexible brain transitions between hierarchical network segregation and integration associated with cognitive performance during a multisource interference task. *IEEE J. Biomed. Heal. Informatics* DOI: https://doi.org/10.1109/JBHI.2021.3119940 (2021).

**68.** Zuberer, A. *et al.* Integration and segregation across large-scale intrinsic brain networks as a marker of sustained attention and task-unrelated thought. *NeuroImage* **229**, 117610, DOI: https://doi.org/10.1016/j.neuroimage.2020.117610 (2021).

**69.** Klinkenberg, I., Sambeth, A. & Blokland, A. Acetylcholine and attention. *Behav. brain research* **221**, 430–442, DOI: https://doi.org/10.1016/j.bbr.2010.11.033 (2011).

**70.** Kowalczyk, N. *et al.* Real-time strategy video game experience and structural connectivity–a diffusion tensor imaging study. *Hum. brain mapping* **39**, 3742–3758, DOI: https://doi.org/10.1002/hbm.24208 (2018).

**71.** Sabri, O. *et al.* Cognitive correlates of $\alpha 4\beta 2$ nicotinic acetylcholine receptors in mild alzheimer's dementia. *Brain* **141**, 1840–1854, DOI: https://doi.org/10.1093/brain/awy099 (2018).

**72.** Ueno, K.-i. *et al.* $\alpha 4\beta 2$ nicotinic acetylcholine receptor activation ameliorates impairment of spontaneous alternation behavior in stroke-prone spontaneously hypertensive rats, an animal model of attention deficit hyperactivity disorder. *J. Pharmacol. Exp. Ther.* **302**, 95–100, DOI: https://doi.org/10.1124/jpet.302.1.95 (2002).

**73.** Howe, W. M. *et al.* Enhancement of attentional performance by selective stimulation of $\alpha$ 4 $\beta$ 2* nachrs: Underlying cholinergic mechanisms. *Neuropsychopharmacology* **35**, 1391–1401, DOI: https://doi.org/10.1038/npp.2010.9 (2010).

**74.** Herzog, R. *et al.* A mechanistic model of the neural entropy increase elicited by psychedelic drugs. *Sci. reports* **10**, 1–12, DOI: https://doi.org/10.1038/s41598-020-74060-6 (2020).

**75.** Coronel-Oliveros, C., Castro, S., Cofré, R. & Orio, P. Structural features of the human connectome that facilitate the switching of brain dynamics via noradrenergic neuromodulation. *Front. Comput. Neurosci.* 61, DOI: https://doi.org/10.3389/fncom.2021.687075 (2021).

**76.** Nghiem, T.-A. E. *et al.* Cholinergic switch between two types of slow waves in cerebral cortex. *Cereb. Cortex* **30**, 3451–3466, DOI: https://doi.org/10.1093/cercor/bhz320 (2020).

**77.** Schliebs, R. & Arendt, T. The cholinergic system in aging and neuronal degeneration. *Behav. brain research* **221**, 555–563, DOI: https://doi.org/10.1016/j.bbr.2010.11.058 (2011).

**78.** Rosas, F. E., Mediano, P. A., Gastpar, M. & Jensen, H. J. Quantifying high-order interdependencies via multivariate extensions of the mutual information. *Phys. Rev. E* **100**, 032305, DOI: https://doi.org/10.1103/PhysRevE.100.032305 (2019).

**79.** Battiston, F. *et al.* Networks beyond pairwise interactions: structure and dynamics. *Phys. Reports* **874**, 1–92, DOI: https://doi.org/10.1016/j.physrep.2020.05.004 (2020).

**80.** Medina-Mardones, A. M., Rosas, F. E., Rodríguez, S. E. & Cofré, R. Hyperharmonic analysis for the study of high-order information-theoretic signals. *J. Physics: Complex.* **2**, 035009, DOI: 10.1088/2632-072X/abf231 (2021).

**81.** Gatica, M. *et al.* High-order functional interactions in ageing explained via alterations in the connectome in a whole-brain model. *bioRxiv* DOI: https://www.biorxiv.org/content/10.1101/2021.09.15.460435v1 (2021).

**82.** Gatica, M. *et al.* High-order interdependencies in the aging brain. *Brain connectivity* DOI: https://doi.org/10.1089/brain.2020.0982 (2021).

**83.** Marchi, M. & Grilli, M. Presynaptic nicotinic receptors modulating neurotransmitter release in the central nervous system: functional interactions with other coexisting receptors. *Prog. neurobiology* **92**, 105–111, DOI: https://doi.org/10.1016/j.pneurobio.2010.06.004 (2010).

**84.** Hansen, E. C., Battaglia, D., Spiegler, A., Deco, G. & Jirsa, V. K. Functional connectivity dynamics: modeling the switching behavior of the resting state. *Neuroimage* **105**, 525–535, DOI: https://doi.org/10.1016/j.neuroimage.2014.11.001 (2015).